



Simplify your imaging workflows

**Make research imaging workflows accessible, traceable,
and secure with Athena Software for Core Imaging Facilities.**

Thermo Scientific™ Athena Software is a premium imaging data management platform designed for core imaging facilities that support materials science research.

Athena Software ensures traceability of images, metadata, and experimental workflows through an intuitive and collaborative web interface.

Find out more at thermofisher.com/athena

ThermoFisher
SCIENTIFIC

Bioinspired Triboelectric Soft Robot Driven by Mechanical Energy

Yuan Liu, Baodong Chen, Wei Li, Lulu Zu, Wei Tang, and Zhong Lin Wang*

A sustainable power source is a key technical challenge for practical applications of electrically responsive soft robots, especially the required voltage is over several thousand volts. Here, a practicable new technology, triboelectric soft robot (TESR) system with the primary characteristics of power source from mechanical energy, is developed. At its heart is TESR with bioinspired architectures made of soft-deformable body and two triboelectric adhesion feet, which is driven and accurately controlled through triboelectric effect, while reaching maximum crawling speeds of 14.9 mm s^{-1} on the acrylic surface. The characteristics of the TESR, including displacement and force, are tested and simulated under the power of a rotary freestanding triboelectric nanogenerator (RF-TENG). Crawling of TESR is successfully realized on different materials surfaces and different angle slopes under the driven of RF-TENG. Furthermore, a real-time visual monitoring platform, in which TESR carries a micro camera to transmit images in a long narrow tunnel, is also achieved successfully, indicating that it can be used for fast diagnosis in an area inaccessible to human beings in the future. This study offers a new insight into the sustainable power source technologies suitable for electrically responsive soft robots and contributes to expanding the applicability of TENGs.

robots can be powered based mainly on the two forms: pressure-driven soft actuators and stimuli-responsive soft actuators.^[4] In general, pressure-driven soft actuators are driven by rigid electric motors or pumps, such as a multi-gait quadruped robots,^[5] an active camouflage-inspired robot,^[6] a snake-inspired locomotion robot,^[7] a remora suckerfish-inspired underwater robot.^[8] Typical stimuli-responsive soft actuators include electrically responsive, magnetically responsive, chemically responsive, thermally responsive, photo-responsive, and etc.^[4] Obviously, various power sources have been used to drive the robots. Some measures have been taken to achieve an untethered soft robotic system based on various power sources. For example, a hydrogen peroxide monopropellant, as well as a high energy density chemical fuel source, is used to generate pressurized gas to drive pressure-driven soft actuators.^[9] An electronically powered liquid crystal elastomer actuator,^[10]

an electronically powered liquid crystal elastomer actuator,^[3] a light-responsive liquid crystal elastomer actuator, and a magnetically actuated soft millimeter scale robot^[11] are designed to achieve an untethered soft robotics. However, power sources, especially for stretchable, portable power sources, is always a big challenge for soft robots.^[2]

Compared to other stimuli-responsive soft actuators, it can be easier for electrically responsive soft actuators to be controlled by electrical signal directly and precisely. Among electrically responsive soft actuator, dielectric elastomer stands out with the characteristics of fast response (on the order of millisecond),

1. Introduction

Soft robots have attracted great attention owing to its unique advantages over conventional rigid robots in recent years, including large deformation, high agility, good flexibility and strong adaptability to environments.^[1] So far, for the development of soft robotic systems, a variety of potential applications has been addressed to locomotion, manipulation and human machine interaction.^[2] In particular, inspired by a range of biological systems, mimicking the agile motions of fish, octopuses, snakes, caterpillar, and worm is very popular.^[3] Currently, soft


Y. Liu, Prof. B. Chen, L. Zu, Prof. W. Tang, Prof. Z. L. Wang
CAS Center for Excellence in Nanoscience
Beijing Key Laboratory of Micro-nano Energy and Sensor
Beijing Institute of Nanoenergy and Nanosystems
Chinese Academy of Sciences
Beijing 101400, P. R. China
E-mail: zhong.wang@mse.gatech.edu

Y. Liu, Prof. B. Chen, L. Zu, Prof. W. Tang, Prof. Z. L. Wang
School of Nanoscience and Technology
University of Chinese Academy of Sciences
Beijing 100049, P. R. China

Prof. B. Chen, Prof. W. Tang
Institute of Applied Nanotechnology
Jiaxing, Zhejiang 314031, P. R. China

Dr. W. Li
State Key Laboratory of Tribology
Department of Mechanical Engineering
Tsinghua University
Beijing 100084, P. R. China

Prof. Z. L. Wang
School of Materials Science and Engineering
Georgia Institute of Technology
Atlanta, GA 30332-0245, USA

 The ORCID identification number(s) for the author(s) of this article can be found under <https://doi.org/10.1002/adfm.202104770>.

DOI: 10.1002/adfm.202104770

large deformation, high energy density, lightweight and self-sensing.^[12] These properties make dielectric elastomers great potential in a wide variety of fields including sensors, energy harvesters, artificial muscles, microfluidics and bioinspired and biomimetic soft robots.^[13] A large number of soft robotic grippers and soft robots with dielectric elastomer actuators have been developed,^[3,13,14] like terrestrial robots, underwater robots, aerial robots, wearable/humanoid robots, wall-climbing robots, et al.^[15] However, a huge challenge remains due to the requirement for high voltages. The power source is generally provided by a relatively heavy and bulky high voltage power supply, which will not be a potential option of power sources in developing an untethered soft robotic system in future.

Triboelectric nanogenerator (TENG) was invented by Z. L. Wang in 2012,^[16] as a promising new technology for harvesting mechanical energy from nature environment and converting it into electricity, which is based on the coupling of the electrostatic induction and the triboelectrification effect.^[17,18] Since then, the applications of TENG have been blooming in these four fields: micro/nano energy,^[19–22] self-powered sensors/systems,^[23–26] large-scale blue energy,^[27–29] and direct high voltage sources.^[30–34] Especially, as a power sources with unique high voltage character, TENG has the ability of driving electrically responsive materials,^[35,36] such as piezoelectric films, liquids,^[37,38] gases,^[33] and dielectric elastomers,^[35] which indicates the TENG can have the potential to power the soft robot. However, few studies have designed a soft robot prototype powered by RF-TENG and achieve the locomotion of this prototype. Therefore, the structure, control module, and characteristics of soft robots powered by TENG have remained unknown and have been a challenge.

In this paper, we present a concept of triboelectric soft robot (TESR) system, in which inchworm-inspired TESR consisting mainly of two electrically responsive materials is combined with TENGs. The locomotion of TESR is driven by mechanical energy. Specifically, the mechanical energy is converted to the high voltage to power TESR through rotary freestanding triboelectric nanogenerator (RF-TENG). Inspired by the locomotion of inchworm, a control module is designed to ensure the coordination of TESR between the soft-deformable body and triboelectric adhesion feet (TAF) to achieve stable crawling. The characteristics of the force and displacement of soft-deformable body, as well as the characteristics of normal force and tangential force of TAF, have been tested under the power of RF-TENG. The displacement and force of soft-deformable body in the experiment suggest a good agreement with that in the simulation. Furthermore, we have demonstrated the capabilities of TESR to crawl on multiple substrates and climb slopes with different angles powered by RF-TENG. Finally, the application of TESR in small space exploration has been demonstrated. This work greatly expands the applicability of TENGs as a new high voltage power source in the field of soft robot.

2. Results

2.1. Structure and Working Principle of TESR

TESR system, including an inchworm-inspired TESR, control module, and RF-TENG, has been developed as shown in

Figure 1a. In this system, TESR with bioinspired architectures consists of a soft-deformable body and two TAF. Powered by RF-TENG, the soft-deformable body produces the deformation and two TAF produce controlled adhesion forces. Detailed structure information of the soft-deformable body is visualized by Figure 1b. To be specific, from top to bottom, the soft-deformable body is composed of a whole flexible acrylic frame (thickness of 0.3mm), a biaxial pre-stretched dielectric elastomer membrane, two half-circular flexible acrylic frame (thickness of 0.3 mm) and a rigid carbon fiber plate (thickness of 0.4 mm). A detailed fabrication procedure of the soft-deformable body is available in the Figure S3 in the Supporting Information. As for soft-deformable body, the dielectric elastomer membrane is pre-stretched biaxially five times using a self-made stretching tool. The middle part of the acrylic frame is used as the loading platform, on which some equipments are put, such as micro cameras.

In this system, RF-TENG provides two high voltage outputs: one high voltage output to the soft-deformable body (output I) and the other high voltage output to TAF (output II). The two-way high voltage outputs RF-TENG are designed to meet the voltage requirements of the soft-deformable body and TAF, respectively. The crawling of TESR based on the locomotion principle of the inchworm involves two processes (shown in Figure 1d). The first process is similar to an anchor-push locomotion of the inchworm. In this stage, the high voltage provided by output I and output II are applied to the soft-deformable body and the left-hand foot, respectively. Thus, the adhesion force between the left-hand foot and substrate is higher than that between right-hand foot and substrate. Since that, the soft-deformable body elongates to push the right-hand foot to move forward (Figure 1d, stage I to stage II). The second process is similar to an anchor-pull locomotion of inchworm. In this system, the high voltage provided by output II is switched from left-hand foot to right-hand foot and output I is turned off, so that the adhesion force between feet and substrate is opposite to stage I. Thus, the soft-deformable body contracts to make TESR crawl forward (Figure 1d, stage II to stage III). In this way, the crawling of TESR is realized. Figure 1f shows that a prototype of TESR crawls a horizontal tunnel (Figure 1f(I,II); Movie S4, Supporting Information) and climbs on inclines with slope of 30 ° (Figure 1f(III,IV); Movie S3, Supporting Information).

To provide sustainable high voltage sources for TESR, RF-TENG has been developed. Detailed structural information of RF-TENG is visualized by Figure 1c. Specifically, RF-TENG consists of two stator part and a rotor part, coaxially assembled. The working principle of RF-TENG is illustrated in Figure 1e. When the rotor is stimulated by mechanical, polyvinyl chloride (PVC) film slips on the paper layer of the stator, and the electrons transfer from the ordinary A4 paper to PVC due to triboelectrification and electrostatic induction.^[16] Freestanding PVC is negatively charged by triboelectrification and simultaneously an equal amount of positive charges are generated on the paper.^[39] Based on the law of charge conservation, the positive charge density of paper is half as much as the negative charge density of PVC.^[32,40] Specifically, at the stage I (Figure 1e), PVC film coincides with the left-hand electrode. Positive charges are induced on the left-hand electrode, with negative charges on the right-hand electrode with no current flowing in the circuit. Then, PVC film

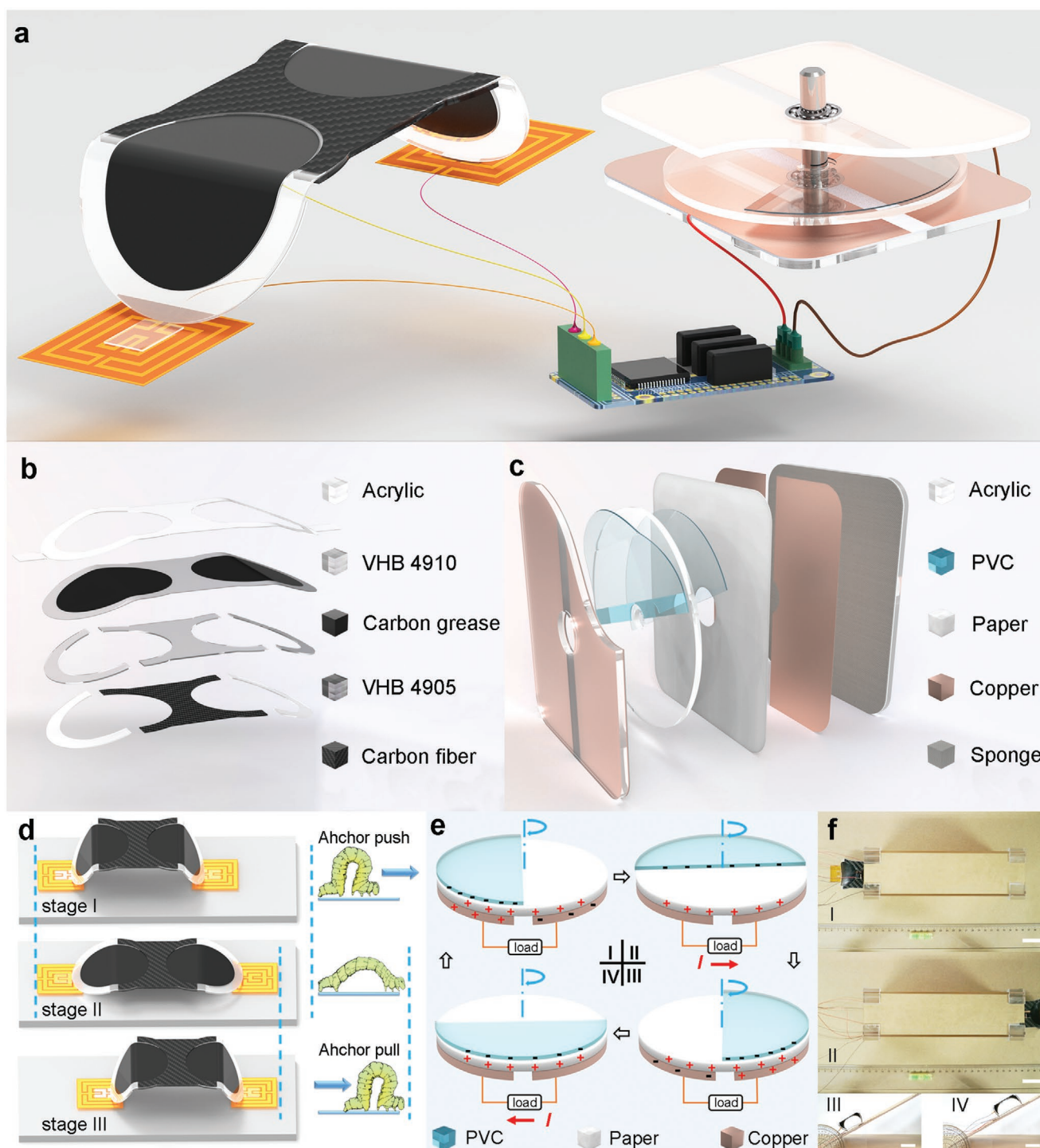


Figure 1. Schematic and application demonstrations of triboelectric soft robot (TESR) system. a) Schematic diagram of TESR system that consists of the TESR, control module and rotary freestanding triboelectric nanogenerator (RF-TENG). b) Exploded view and special components of soft-deformable body. c) Sketch of the basic structure and special components of RF-TENG. d) Schematic of crawling process of TESR based on the locomotion principle of inchworm. e) Working principle of RF-TENG in one cycle. f) The application demonstrations of TESR: crawling into a horizontal tunnel (I, II, scale bar of 30 mm) and on an inclined plane (III, IV, scale bar of 25 mm).

rotates 90° clockwise into stage II. In the stage II, the electrons flow from the right-hand electrode to the left-hand electrode, leading to the current flowing to the right-hand. At this moment,

the net charge of each electrode becomes zero. PVC film keeps rotating until it reaches the right-hand side of the paper completely (Figure 1e, stage III), and the charges on each electrode

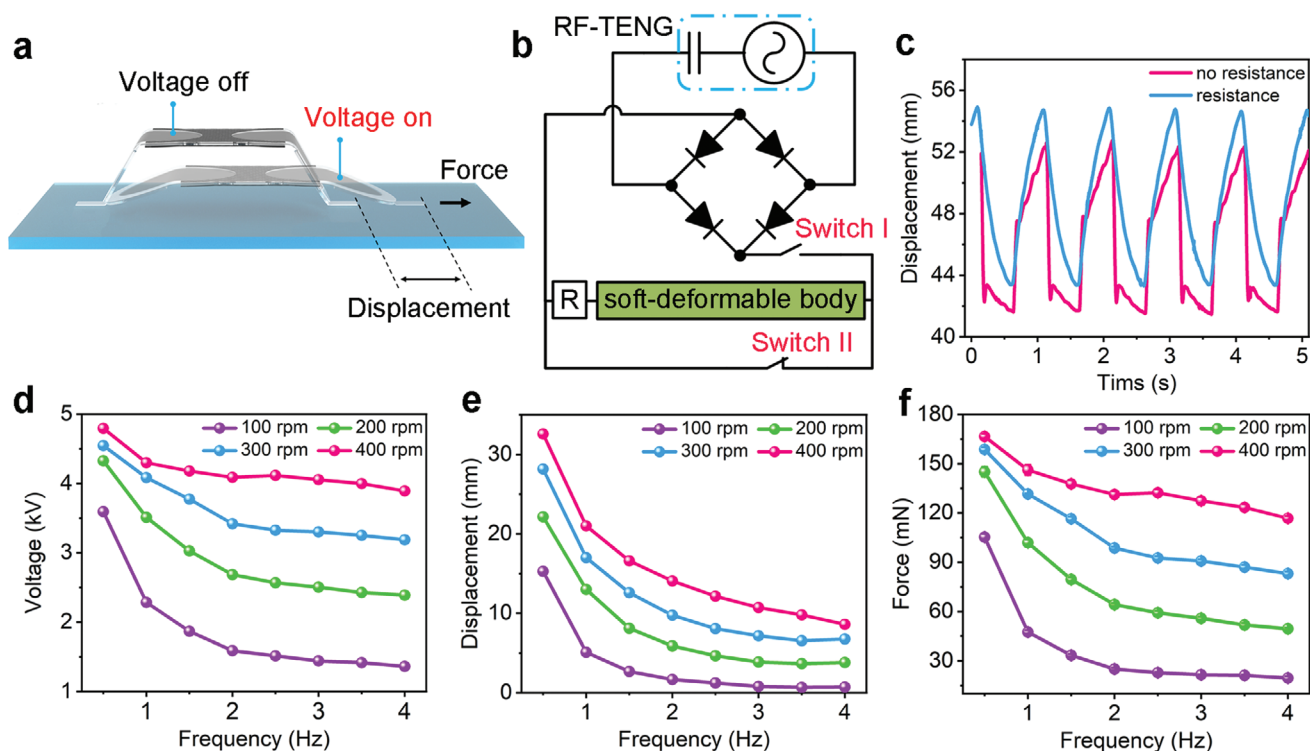


Figure 2. Running characteristics of the soft-deformable body. a) The schematic diagram of displacement and force generated by the soft-deformable body. b) The schematic circuit diagram of soft-deformable body. c) The displacement-time curve of soft-deformable body without resistance or with resistance. The characteristics curves of soft-deformable body powered by RF-TENG at different switching frequencies and rotary speeds: d) the voltage, e) the displacement, and f) the force.

are opposite to the stage I. At the stage IV the charges on each electrode become zero and the current in the circuit flows from right-hand to left-hand. Therefore, a periodic alternating high voltage is generated by the cycling movement of the rotator.

2.2. Running Characterization of the TESR Powered by RF-TENG

2.2.1. Soft-Deformable Body

In order to investigate soft robot driven by RF-TENG, we have tested the basic characteristics of the TESR, including the soft-deformable body and TAF. As shown in **Figure 2a**, the soft-deformable body has an initial length with no voltage. With the high voltage, the soft-deformable body deforms to produce force and displacement under the constraints of the special frames. To quantify the relationship between force and voltage, as well as between displacement and voltage, the driver circuit has been designed as shown in **Figure 2b**. When switch I is activated, soft-deformable body powered by RF-TENG will extend (**Figure 2a**, voltage on), and that switch II is activated, it will resume to original shape (**Figure 2a**, voltage off). The detailed descriptions of the driver circuit are illustrated in **Figure S5** in the Supporting Information.

In the initial testing, the tremor of soft-deformable body occurs, which is extremely detrimental to the crawling of TESR. To remedy this issue, a resistor in series with the soft-deformable body is added to the drive circuit to improve the tremor during the locomotion of TESR. The real-time displacement

curves of the soft-deformable body powered by RF-TENG with or without resistance in the driver circuits are shown in the **Figure 2c**. As we can see, the blue curve is much smoother than the red curve. The result reflects that the resistance, which series in the driver circuit, has a superduper effect on reducing the tremor during locomotion of TESR. The voltage applied on the soft-deformable body is determined by the rotary speed of RF-TENG and the switching frequency of the control module. With RF-TENG at the rotary speeds from 100 to 400 rpm, the output voltages in the different switching frequencies shows corresponding decreasing trends (**Figure 2d**). Moreover, the displacement and the force of soft-deformable body are controlled by the output voltage of RF-TENG. As seen in **Figure 2e,f**, the displacement and force of soft-deformable body decrease as the driving frequency of the control module increases under the power of RF-TENG at the rotary speeds from 100 to 400 rpm. Obviously, the reduction of the voltage applied on the soft-deformable body causes the decrease of force and displacement.

2.2.2. Triboelectric Adhesion Foot (TAF)

The relationship between adhesion forces and the triboelectricity (actually refers to the output voltage produced by RF-TENG) applied on the TAF has also been further investigated, especially when TAF move on different surfaces (wood, release paper, acrylic, copper, etc.). The schematic description of the adhesion of TAF are shown in **Figure 3a**, which consists mainly

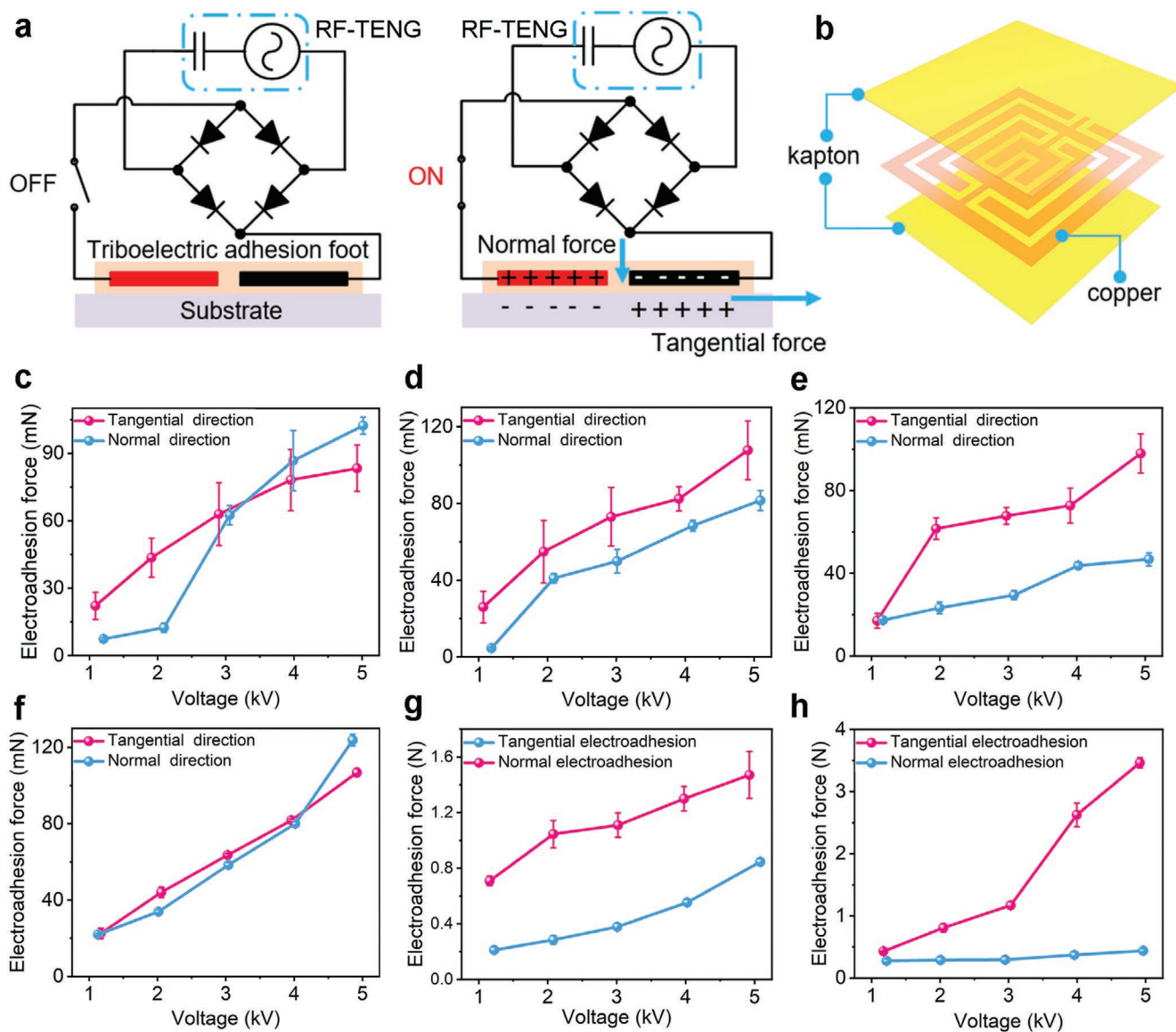


Figure 3. Characteristics of TAF powered by RF-TENG. a) Schematic illustration of the tangential force and normal force generated by triboelectric adhesion feet as controllable anchoring under the power of RF-TENG. b) Exploded-view of the triboelectric adhesion feet. c–h) Tangential force and normal force of the TAF on different substrates: c) release paper I, d) wood, e) abrasive paper, f) acrylic, g) copper, h) release paper II.

of RF-TENG and a full-wave rectifier circuit. The full-wave rectifier circuit can convert the alternating-current into direct high voltage to drive TAF. The high voltage after the full-wave rectifier circuit is connected to the two poles of the interdigitated electrodes. When the switch is turned on, the high voltage across the interdigitated electrodes induce the opposing surface charges of the substrate to produce an attractive force between TAF and substrate surfaces.^[41,42] The attractive force in the tangential direction is called tangential force, and the attractive force in the normal direction is called normal force (Figure 3a). The maximum power consumption of TAF is on the grade of μW , which is driven easily by RF-TENG.

Exploded view of the triboelectric adhesion foot is shown in Figure 3b. The TAF consists of interdigitated electrodes (made

up of copper with a thickness of $175\ \mu\text{m}$) with fantastic adhesive performance^[41] and two Kapton (polyimide) insulating film (thickness of $0.05\ \text{mm}$). The detailed fabrication procedure of TAF is available in Experimental Section.

The normal and tangential direction adhesion forces between TAF and different substrates (release paper I, II, wood, abrasive paper, acrylic, copper) are measured with the different voltages produced by RF-TENG, ranging from 1 to 5 kV. The experimental results are shown in Figure 3c–h (more details of the experiments can be found in the Figure S9 in the Supporting Information). It can be seen that the normal and tangential forces increase in accord with the increase of the applied triboelectricity, and that the tangential force is larger than the normal force in most cases.

2.2.3. Simulation of Force and Displacement Generated by Soft-Deformable Body

To verify the accuracy of experimental results, we use the commercial finite element analysis (FEA) software ABAQUS to carry out the simulation of force and displacement of soft-deformable body. In the simulation, a Neo-Hookean material model, as one of hyperelastic material models, is chosen to carry out the analyses of the deformation of dielectric elastomer membrane. The material properties and the other details of the simulation are shown in Text S1 in the Supporting Information. The initial stresses of dielectric elastomer membrane pre-stretched biaxially, are acquired using FEA. The acquired initial stresses are used to further simulate the deformation of the soft-deformable body, which shows a good agreement of the experimental result (shown in Figure S10 in the Supporting Information). The applied voltage causes the charge transfer from one electrode to another electrode, forming an electric field in the dielectric elastomer membrane. Considering the membrane is thin enough (0.04 mm), the dielectric elastomer membrane with two electrodes is considered as a deformable plate capacitor. Therefore, an effective stress (also called Maxwell stress) results in the deformation of dielectric elastomer membrane in the direction of membrane thickness Z and radial direction R . According to Ref.^[43,44] the stress σ_z in the membrane thickness and the stress σ_r in the radial direction are calculated as follows

$$\sigma_z = -\frac{1}{2} \epsilon_0 \epsilon_r \left(\frac{U}{Z}\right)^2 \quad (1)$$

$$\sigma_r = \frac{1}{2} \epsilon_0 \epsilon_r \left(\frac{U}{Z}\right)^2 \quad (2)$$

Where ϵ_0 , ϵ_r indicates the free-space permittivity ($8.854 \times 10^{-12} \text{ F m}^{-1}$) and relevant dielectric constant of the dielectric elastomer membrane, respectively. U indicates the electric field, which refers to the output voltage produced by RF-TENG. Z indicates the thin of dielectric elastomer membrane.

In the simulation, the stress of dielectric elastomer membrane caused by the applied voltage is simplified to the distributed force of the outer surface in the thickness and radial direction. The distributed force of each mesh of dielectric elastomer membrane is estimated as follows

$$p_z = \sigma_z \quad (3)$$

$$p_r = \sigma_r \quad (4)$$

Where p_z , p_r refers to the distributed force in the thickness and radial direction, respectively.

To explain why carbon fiber plate is chosen as the lower layer of TESR rather than acrylic plate, the displacement of soft-deformable body with acrylic plate and that with carbon fiber plate (see in Figure 4aI) powered by RF-TENG are simulated. The displacement in the vertical direction is represented by height in the Figure 4bII and Figure 4aIII. We can find the fluctuation range of the displacement of carbon fiber plate in

the vertical direction ($-1.316\text{e-}2 \text{ mm}$ – $-2.472\text{e-}3 \text{ mm}$) is within that of acrylic plate in the vertical direction ($-1.851\text{e-}2 \text{ mm}$ – $-2.874\text{e-}3 \text{ mm}$). The fluctuation range ratio δ in vertical direction of carbon fiber plate compared to acrylic plate is described as follows

$$\delta = \frac{\text{flu_range}_c}{\text{flu_range}_A} \times 100\% = 68.4\% \quad (5)$$

Where flu_range_c , flu_range_A refers to the fluctuation range in vertical direction of carbon fiber plate and that of acrylic plate. The result indicates that acrylic plate produces bigger displacement than carbon fiber plate in the vertical direction, which indicates that the soft-deformable body with carbon fiber plate can emerge a bigger tremor than that with acrylic plate in the locomotion of TESR. Besides, taking the rotary speed of 400 rpm as an instance, we simulate the displacement and the force of the soft-deformable body powered by RF-TENG. The simulation results suggest that the curves of force and time at the switching frequency of 1, 2, 3, and 4 Hz have a good agreement of the experimental results, as shown in Figure 4b–e. The relative error rates of maximum force at the frequency of 1, 2, 3, and 4 Hz are 0.08%, 0.09%, 2.85%, and 3.24%, respectively, as shown in Figure 4f. Besides, the maximum value of the displacement in the simulation also shows a good agreement of the experimental results, as shown in Figure 4g. The relative error rates of maximum displacement at the frequency of 1, 2, 3, and 4 Hz are 1.83%, 4.54%, 6.02%, and 13.4%, respectively.

2.3. Locomotion Characteristics of TESR

The locomotion of TESR is produced through a synergy between the deformation of the soft-deformable body and the adhesion of TAF. Therefore, we design a multichannel high voltage control module. The detailed component description of control module is illustrated in Figure S11 in the Supporting Information. The control module consists of a Microcontroller Unit (MCU, STM32F407), a power amplifier board with six channels, and six high voltage reed relays. The periodic step function signals with repeated T (Figure 5a), which are generated by the MCU, are used to control the high voltage reed relays to realize the switching between open and closed of the drive circuit. Based on this, the soft-deformable body and TAF can be activated by turn in a certain timing sequence to achieve the locomotion of TESR.

The capability to locomotion of TESR without being hindered by different substrate or steep gradients is particularly important. To demonstrate TESR prototype's ability, two types of experiments are designed: climbing inclined planes with different slopes and crawling on different substrates. According to Figure 2d–f, the displacement and force of the soft-deformable body are maximum under the power of RF-TENG with the rotary speed of 400 rpm. Hence, the rotary speed of 400 rpm is chosen to achieve the best locomotion performance of TESR. Figure 5c shows the process of TESR climbing along inclined plane with the slope of 30°. The crawling characteristics of TESR on horizontal substrate with release paper I surface under the controlling frequency of 1 Hz are demonstrated in Figure 5d.

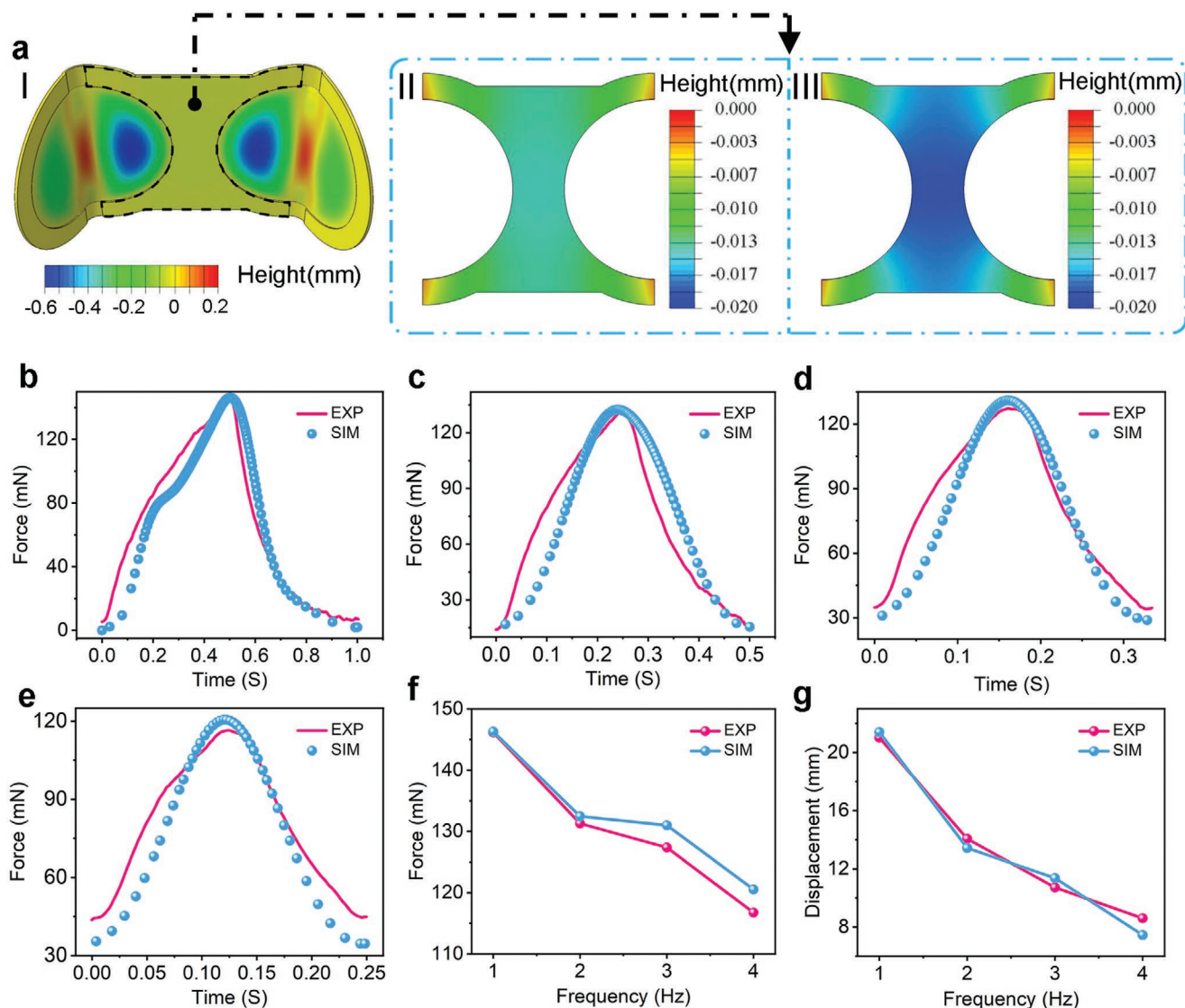


Figure 4. The results of simulation of the soft-deformable body. a) The simulated displacement of soft-deformable body in the vertical direction powered by RF-TENG: I) the displacement of soft-deformable body with carbon fiber plate, II) the displacement of carbon fiber plate of soft-deformable body, and III) the displacement of acrylic plate of soft-deformable body. The force curve of soft-deformable body at the different switching frequency in the simulation and experiment: b) 1 Hz, c) 2 Hz, d) 3 Hz, e) 4 Hz. The curves of two characteristics of soft-deformable body at the different switching frequencies in the simulation and experiment: f) the maximum forces, g) the maximum displacements.

The inset shows the real-time voltage applied to the soft-deformable body. The crawling process of TESR on different substrates under different frequencies are shown in Movie S1 in the Supporting Information. The climbing on the inclined plane with a series of slopes (10° , 20° and 30°) are recorded in Movie S3 in the Supporting Information. The ability of TESR to crawling back and forth on a horizontal substrate has also been demonstrated (Movie S2, Supporting Information).

The crawling speed of TESR can be controlled by regulating the frequency of soft-deformable body and TAF. Therefore, we characterize the relationship between the crawling speed under different horizontal substrate and the control frequency through a micro laser distance sensor, as shown in the Figure 5b (more detail of the experiment is shown in Figure S12 in the Supporting Information). We find that the crawling speed of TESR on each

substrate showed the consistent trend: the speed increase from 1 to 2 Hz, then decrease from 2 to 3 Hz, and finally increase from 3 to 4 Hz. The control frequency and the extension length of soft-deformable body are the major factors that affect the crawling speed of TESR. Based on the fact that the extension length of soft-deformable body increased with the control frequency increasing before saturation of viscoelastic damping response.^[45] The maximum speed of TESR reach 14.9 mm s^{-1} at the control frequency of 2.0 Hz under the acrylic surface in this study.

2.4. A Real-Time Visual Monitoring Performance of TESR

The basic capability and multi-surface adaptability of TESR prototype have been demonstrated in previous sections. In this

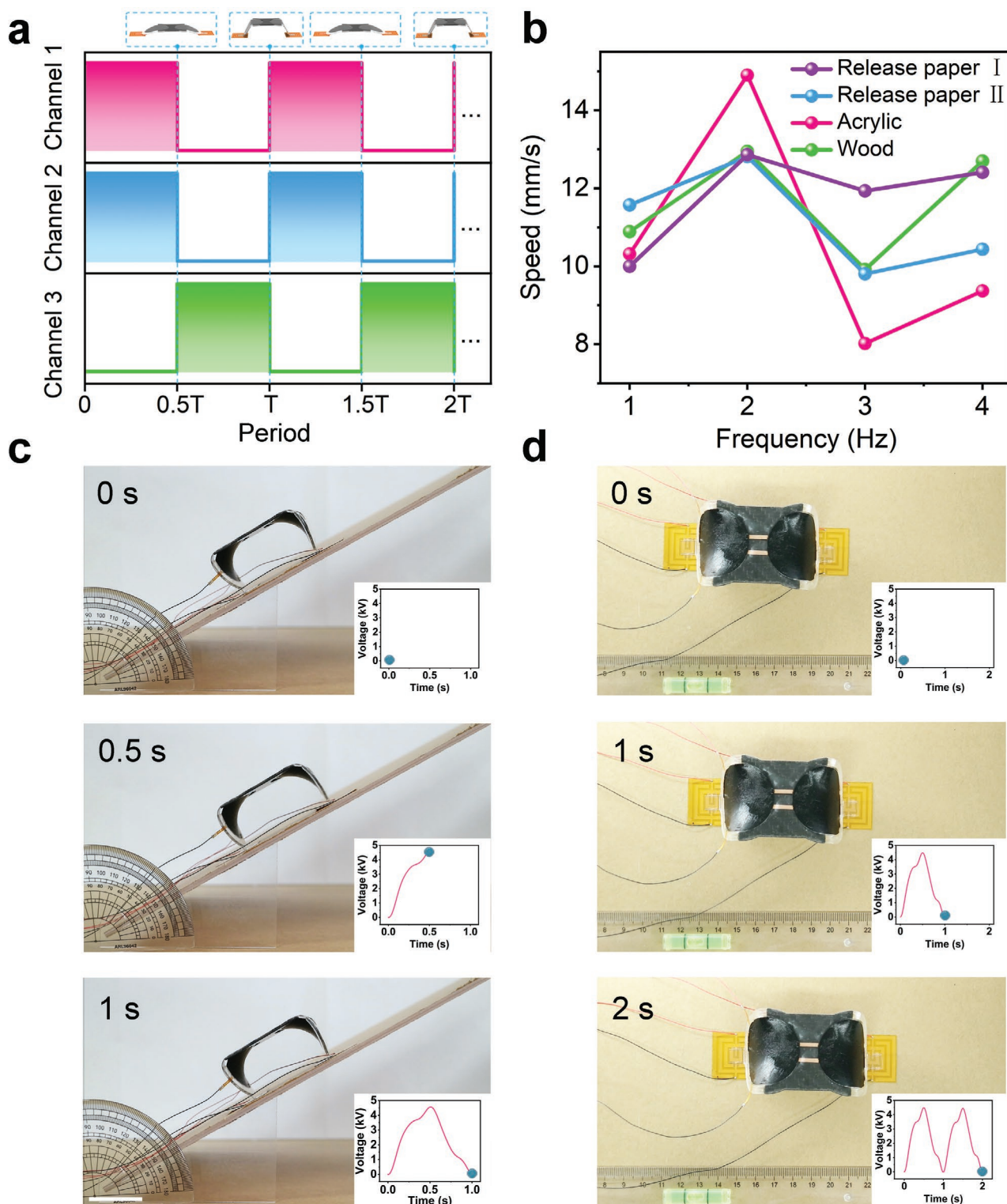


Figure 5. Locomotion characteristics of TESR under different conditions. a) Control pattern of TESR with three channel signals. b) Peristalsis speed of the TESR varying with the frequencies of control signals under different substrates. c, d) Photograph of the climbing process of the TESR on the inclined planes with slopes of 30° (scale bar of 25 mm) and on the horizontal planes.

section, we further demonstrate a real-time visual monitoring platform based on TESR. Specifically, a TESR prototype is used to explore narrow spaces (Figure 6a, horizontal tunnel; length

of 200 mm, width of 50 mm, height of 97 mm) and transfer the images in the spaces to the computer in real time. To that end, a micro camera (weight of 1 g, size of 6 × 6 × 6 mm, model

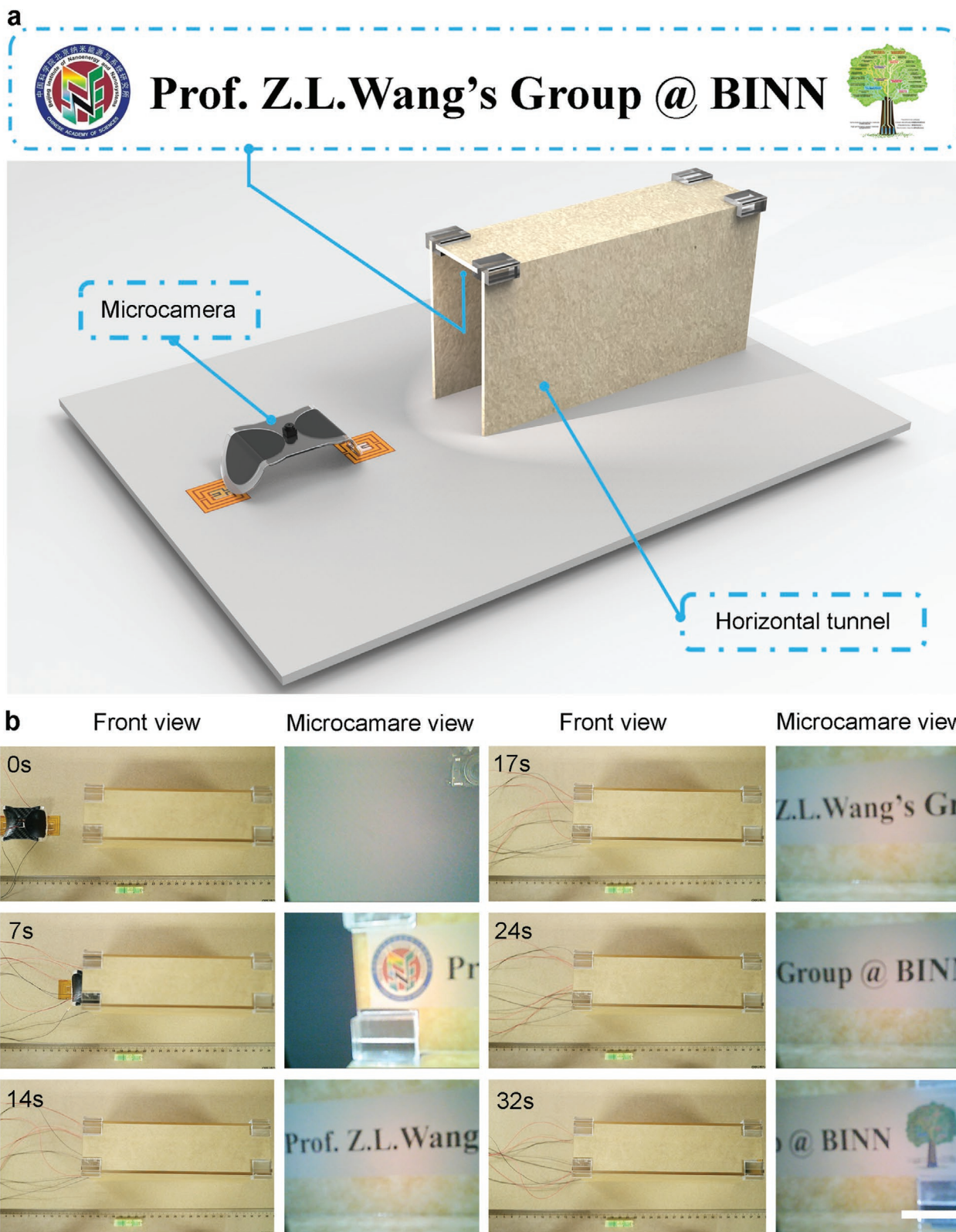


Figure 6. Demonstration of the video recording function of TESR in a cabined horizontal tunnel. A prototype of TESR carry onboard micro camera crawling into a horizontal tunnel (length, 200 mm; width, 50 mm; height, 97 mm) to record images: the logo of BINN, “Prof. Z. L. Wang’s Group @ BINN”, Prof. Z. L. Wang’s tree. a) Schematic illustration of the demonstration. b) The process of the tunnel crawling and onboard micro camera recording images of TESR (scale bar of 20 mm).

RS-406C32-3.3V, 1/4 inch HD color CMOS) as an onboard recording device is installed on the TESR prototype. As seen in Figure 6 and Movie S4 (Supporting Information), the TESR prototype climbs autonomously into the horizontal tunnel and transmits the image of the upper part of the tunnel through the onboard micro camera. According to Figure 6b, it takes about 25 seconds for TESR to pass through the horizontal tunnel with the length of 200 mm.

3. Conclusion

In summary, we have presented the TESR, a bio-inspired soft robot powered by RF-TENG capable of crawling autonomously and performing simple tasks. Owing to its unique structural design, TESR prototype has good adaptability of crawling on different substrates. As the main components of TESR, the characteristics of the soft-deformable body and TAF are analyzed under the power of RF-TENG. Specifically, the force and displacement generated by soft-deformable body are measured under different controlled frequencies, respectively. Meanwhile, the adhesion forces between TAF and different substrates are measured under different triboelectricity. Under the control of MCU, two TAF and soft-deformable body are activated in sequence to realize the locomotion of TESR. Moreover, the maximum crawling speed is obtained on the acrylic substrate which is 14.9 mm s^{-1} . Our work focuses on exploring a soft robot powered by harvesting mechanical energy. This work offers a promising, facile, and safe power source as a supplement to traditional soft robot, and will enrich the diversity of TENGs applications based on the reach of existing technologies.

4. Experimental Section

Structural Design and Fabrication Process of RF-TENG: RF-TENG consists of three main components, one rotator and two stators. The PVC (thickness of $120 \mu\text{m}$) and the paper (thickness of $110 \mu\text{m}$) are used as the friction materials. The stator consists of paper, sponge, electrodes and acrylic board. As the positive friction materials, the paper with copper electrodes (thickness of $200 \mu\text{m}$) was fixed on the stator. The gap between positive and negative electrodes was 10 mm. The rotor was composed of acrylic board and PVC film. Acrylic board (thickness of 6 mm) was processed by numerical control machine tool to ensure the perpendicularity of the center hole to achieve good parallelism between the surfaces of two friction materials. Thus, the friction materials can fit closely to obtain good output performance. After processing, the acrylic board with a center mounting hole was a circle with a diameter of 210 mm, a circle PVC film was cut manually into semicircle with diameter of 200 mm on the semicircular acrylic template. Then, two semicircular PVC film was pasted on both sides of the circular acrylic board using Teflon tape. As a cushioning material, a sponge was used to improve the fitness of the friction material, sandwiched by electrodes and acrylic board. The countersunk hole of motor connection board was used to connect the motor and stator, which ensures no gap between them. The relative position relationship between rotor and motor, as well as between stator and motor was determined by the shaft sleeve and the motor shaft, so that, the pressure between the two friction materials remains the same in each assembly.

Structural Design and Fabrication Process of TESR Prototypes: The soft-deformable body, which actually refers to dielectric elastomer actuator, which was made of VHB 4910, 4905 (3M company), carbon grease (846-80G, MG Chemical), acrylic board (thickness 0.3mm) and

carbon fiber (thickness of 0.4 mm). The fabrication process of dielectric elastomer actuator was available in the Figure S3 in the Supporting Information. The TAF was made from flexible circuit board technology. Interdigitated electrodes and two Kapton insulating film were combined by hot pressing process. The top Kapton film insulates the interdigitated electrodes surface and the bottom Kapton film was acted as a dielectric medium layer.

Characterization Method of Soft-Deformable Body Voltage: The voltage applied to soft-deformable body was measured by Keithley 6517 electrometer and the measuring circuit was shown in Figure S6a in the Supporting Information. Keithley 6517 electrometer was used as an ammeter in series with a resistor ($110 \text{ G}\Omega$) to measure the voltage on the soft-deformable body, considering that the measured voltage exceeds the maximum range of the electrometer voltage range. The experiment process was available in the Figure S6 in the Supporting Information.

Characterization Method of Soft-Deformable Body Displacement: The soft-deformable body was placed on a horizontal plane. A micro laser distance sensor (HG-C1400, measurement range of 400 mm, repeatability of $300 \mu\text{m}$, Panasonic), which was installed on a Z-axis translation stage, was used to record the displacement of soft-deformable body. We fix one hinge on the substrate was fixed and the other hinge was kept active, and an L-shape baffle plate was adhered to the freely hinge to provide a reflective surface for micro laser distance sensor. The experiment process was available in the Figure S7 in the Supporting Information.

Characterization Method of Soft-Deformable Body Force: The soft-deformable body was placed on a horizontal plane. One hinge was fixed on the plane and fix the other hinge on a one-dimensional force sensor (SBT630, rated load 2N) which was installed on a Z-axis translation stage. The measured process of the force could be described as the following step. The soft-deformable body was connecting to the high voltage control module and RF-TENG. The soft-deformable body will work and the one-dimensional force sensor will capture the force signals which are generated by soft-deformable body with 10s. The above steps will be repeated until all experiments were completed. The experiment process is available in Figure S8 in the Supporting Information.

Characterization Method of Adhesion Forces: TAF was placed on different substrates. A one-dimensional force sensor (SBT630, rated load 2N, 5N), which was installed on a linear motor (BF01-37, LinMot), was used to measure the adhesion force. The measured process of the tangential adhesion force was described as the following step: firstly, we use a soft rope was used to connect TAF with force sensor. Secondly, the triboelectricity was applied to TAF. After two seconds, TAF moves horizontally at a constant speed of 1 mm s^{-1} , which was generated by the linear motor. The force was recorded by the force sensor in real time. Thirdly, when the linear motor displacement reaches 10 mm, the measurement stops. The normal adhesion force was measured as the same measurement procedure above. The key difference was that the linear motor needs to provide vertical movement. The experiment process is available in Figure S9 in the Supporting Information.

Supporting Information

Supporting Information is available from the Wiley Online Library or from the author.

Acknowledgements

Y.L., B.C., and W.L. contributed equally to this work. The authors acknowledge the support from Beijing Natural Science Foundation (Grant Nos. 2192062), supported by National Natural Science Foundation of China (Grant Nos. 51502147, 51702018, and 11704032). The research was sponsored by the National Key R & D Project from Minister of Science and Technology (2016YFA0202704), and the Beijing Municipal Science and Technology Commission (Z181100003818016 and Y3993113DF).

Conflict of Interest

The authors declare no conflict of interest.

Data Availability Statement

Research data are not shared.

Keywords

bioinspired soft robots, mechanical energy harvesting, sustainable power sources, triboelectric nanogenerators

Received: May 19, 2021

Revised: June 18, 2021

Published online:

-
- [1] N. Kellaris, V. G. Venkata, G. M. Smith, S. K. Mitchell, C. Keplinger, *Sci. Rob.* **2018**, *3*, eaar3276.
- [2] D. Rus, M. T. Tolley, *Nature* **2015**, *521*, 467.
- [3] T. Li, G. Li, Y. Liang, T. Cheng, J. Dai, X. Yang, B. Liu, Z. Zeng, Z. Huang, Y. Luo, *Sci. Adv.* **2017**, *3*, 1602045.
- [4] L. Hines, K. Petersen, G. Z. Lum, M. Sitti, *Adv. Mater.* **2017**, *29*, 1603483.
- [5] R. F. Shepherd, F. Ilievski, W. Choi, S. A. Morin, A. A. Stokes, A. D. Mazzeo, X. Chen, M. Wang, G. M. Whitesides, *Proc. Natl. Acad. Sci. USA* **2011**, *108*, 20400.
- [6] S. A. Morin, R. F. Shepherd, S. W. Kwok, A. A. Stokes, A. Nemiroski, G. M. Whitesides, *Science* **2012**, *337*, 828.
- [7] C. D. Onal, D. Rus, *Bioinspiration Biomimetics* **2013**, *8*, 026003.
- [8] Y. Wang, X. Yang, Y. Chen, D. K. Wainwright, C. P. Kenaley, Z. Gong, Z. Liu, H. Liu, J. Guan, T. Wang, *Sci. Rob.* **2017**, *2*, eaan8072.
- [9] M. Wehner, M. T. Tolley, Y. Mengüç, Y.-L. Park, A. Mozeika, Y. Ding, C. Onal, R. F. Shepherd, G. M. Whitesides, R. J. Wood, *Soft Rob.* **2014**, *1*, 263.
- [10] Q. He, Z. Wang, Y. Wang, A. Minori, M. T. Tolley, S. Cai, *Sci. Adv.* **2019**, *5*, eaax5746.
- [11] W. Hu, G. Z. Lum, M. Mastrangeli, M. Sitti, *Nature* **2018**, *554*, 81.
- [12] G.-Y. Gu, J. Zhu, L.-M. Zhu, X. Zhu, *Bioinspiration Biomimetics* **2017**, *12*, 011003.
- [13] C. Christianson, N. N. Goldberg, D. D. Deheyn, S. Cai, M. T. Tolley, *Sci. Rob.* **2018**, *3*, eaat1893.
- [14] E.-F. M. Henke, S. Schlatter, I. A. Anderson, *Soft Rob.* **2017**, *4*, 353.
- [15] U. Gupta, L. Qin, Y. Wang, H. Godaba, J. Zhu, *Smart Mater. Struct.* **2019**, *28*, 103002.
- [16] F.-R. Fan, Z.-Q. Tian, Z. L. Wang, *Nano Energy* **2012**, *1*, 328.
- [17] Z. L. Wang, *Nano Energy* **2020**, *68*, 104272.
- [18] G. Zhu, J. Chen, T. Zhang, Q. Jing, Z. L. Wang, *Nat. Commun.* **2014**, *5*, 3426.
- [19] Z. Yang, Y. Yang, F. Liu, Z. Wang, Y. Li, J. Qiu, X. Xiao, Z. Li, Y. Lu, L. Ji, Z. L. Wang, J. Cheng, *ACS Nano* **2021**, *15*, 2611.
- [20] J. Zhong, Y. Zhang, Q. Zhong, Q. Hu, B. Hu, Z. L. Wang, J. Zhou, *ACS Nano* **2014**, *8*, 6273.
- [21] J. Wang, S. Li, F. Yi, Y. Zi, J. Lin, X. Wang, Y. Xu, Z. L. Wang, *Nat. Commun.* **2016**, *7*, 12744.
- [22] H. S. Wang, C. K. Jeong, M.-H. Seo, D. J. Joe, J. H. Han, J.-B. Yoon, K. J. Lee, *Nano Energy* **2017**, *35*, 415.
- [23] Z. Wang, J. An, J. Nie, J. Luo, J. Shao, T. Jiang, B. Chen, W. Tang, Z. L. Wang, *Adv. Mater.* **2020**, *32*, 2001466.
- [24] J. An, Z. Wang, T. Jiang, P. Chen, X. Liang, J. Shao, J. Nie, M. Xu, Z. L. Wang, *Mater. Today* **2020**, *41*, 10.
- [25] J. Luo, Z. Wang, L. Xu, A. C. Wang, K. Han, T. Jiang, Q. Lai, Y. Bai, W. Tang, F. R. Fan, Z. L. Wang, *Nat. Commun.* **2019**, *10*, 5147.
- [26] Y. Peng, M. Que, H. E. Lee, R. Bao, X. Wang, J. Lu, Z. Yuan, X. Li, J. Tao, J. Sun, *Nano Energy* **2019**, *58*, 633.
- [27] Y. Feng, T. Jiang, X. Liang, J. An, Z. L. Wang, *Appl. Phys. Rev.* **2020**, *7*, 021401.
- [28] Y. Feng, X. Liang, J. An, T. Jiang, Z. L. Wang, *Nano Energy* **2021**, *81*, 105625.
- [29] X. Liang, T. Jiang, G. Liu, Y. Feng, C. Zhang, Z. L. Wang, *Energy Environ. Sci.* **2020**, *13*, 277.
- [30] H. Huo, F. Liu, Y. Luo, Q. Gu, Y. Liu, Z. Wang, R. Chen, L. Ji, Y. Lu, R. Yao, *Nano Energy* **2020**, *67*, 104150.
- [31] A. Li, Y. Zi, H. Guo, Z. L. Wang, F. M. Fernández, *Nat. Nanotechnol.* **2017**, *12*, 481.
- [32] C. Li, Y. Yin, B. Wang, T. Zhou, J. Wang, J. Luo, W. Tang, R. Cao, Z. Yuan, N. Li, *ACS Nano* **2017**, *11*, 10439.
- [33] J. Cheng, W. Ding, Y. Zi, Y. Lu, L. Ji, F. Liu, C. Wu, Z. L. Wang, *Nat. Commun.* **2018**, *9*, 3733.
- [34] H. Guo, J. Chen, L. Wang, A. C. Wang, Y. Li, C. An, J. He, C. Hu, V. K. Hsiao, Z. L. Wang, *Nat. Sustain.* **2021**, *4*, 147.
- [35] X. Chen, T. Jiang, Y. Yao, L. Xu, Z. Zhao, Z. L. Wang, *Adv. Funct. Mater.* **2016**, *26*, 4906.
- [36] J. Wang, C. Meng, Q. Gu, M. C. Tseng, S. T. Tang, H. S. Kwok, J. Cheng, Y. Zi, *ACS Nano* **2020**, *14*, 3630.
- [37] L. Zheng, Y. Wu, X. Chen, A. Yu, L. Xu, Y. Liu, H. Li, Z. L. Wang, *Adv. Funct. Mater.* **2017**, *27*, 1606408.
- [38] J. Nie, Z. Ren, J. Shao, C. Deng, L. Xu, X. Chen, M. Li, Z. L. Wang, *ACS Nano* **2018**, *12*, 1491.
- [39] H. Zou, Y. Zhang, L. Guo, P. Wang, X. He, G. Dai, H. Zheng, C. Chen, A. C. Wang, C. Xu, Z. L. Wang, *Nat. Commun.* **2019**, *10*, 1427.
- [40] G. Zhu, J. Chen, T. Zhang, Q. Jing, Z. L. Wang, *Nat. Commun.* **2014**, *5*, 3426.
- [41] M. Graule, P. Chirattananon, S. Fuller, N. Jafferis, K. Ma, M. Spenko, R. Kornbluh, R. Wood, *Science* **2016**, *352*, 978.
- [42] R. Liu, R. Chen, H. Shen, R. Zhang, *Int. J. Adv. Rob. Syst.* **2013**, *10*, 36.
- [43] Z. Suo, *Acta Mech. Solida Sin.* **2010**, *23*, 549.
- [44] M. Wissler, E. Mazza, *Sens. Actuators, A* **2007**, *138*, 384.
- [45] K. M. Digumarti, C. Cao, J. Guo, A. T. Conn, J. Rossiter, presented at *2018 IEEE Int. Conf. on Soft Robotics (RoboSoft)*, IEEE, Piscataway, NJ **2018**.